# Evolution of Fe-rich intermetallics in Al-Si-Cu 319 cast alloy with various Fe, Mo, and Mn contents

Lanfeng Jin, Kun Liu*, X. Grant Chen

Department of Applied Science, University of Quebec at Chicoutimi, Saguenay, QC G7H 2B1, Canada

*Corresponding author: kun.liu@uqac.ca; Tel.: 1-4185455011 ext.7112; Fax: 1-4185455012

**Abstract:**

In the present work, the precipitation and preferential selection of Fe-rich intermetallics in Al-Si-Cu 319 cast alloys with two Fe contents (0.3 and 0.7 wt.%) and various Mo contents (0-0.4 wt.%) were investigated. The results showed that two types of platelet β-Fe (defined as eutectic β-Fe and pre-eutectic β-Fe) and α-Fe can precipitate depending on the alloy compositions, such as the Fe and Mo contents. Generally, the addition of Mo promotes the formation of α-Fe instead of β-Fe. However, its effect on the phase competition between β-Fe and α-Fe is greatly related to the Fe content. In alloys with low Fe content (0.3%), an addition of 0.37% Mo can promote the complete precipitation of α-Fe and suppress the formation of eutectic β-Fe. However, in alloys with high Fe content (0.7%), only the pre-eutectic β-Fe amount decreases with increasing Mo addition, leaving the eutectic β-Fe almost unchanged. While both pre-eutectic β-Fe and eutectic β-Fe can be fully suppressed with a combined addition of Mn (0.24%) and Mo (0.4%). Compared with Mn, Mo exhibits a stronger effect on the promotion of α-Fe. The combined addition of Mn and Mo can achieve better modifications of both pre-eutectic and eutectic β-Fe in 319 alloys with high Fe content.

**Keywords:** Al-Si-Cu 319 cast alloy; Fe-rich intermetallics; Mo; Phase selection.

## 1. Introduction:

Al-Si cast alloys have attracted much attention in the automotive industry owing to their excellent castability and combination of strength and ductility. Further, their high strength-to-weight ratio, high thermal conductivity, and good machinability make them perfect candidates for various manufacturing areas and technology fields [1-3]. In aluminum cast alloys, Fe is often regarded as the most common but inevitable impurity

because it can be easily introduced but difficult and expensive to be removed in the commercial practice [4-5]. Various Fe-rich intermetallics can precipitate during solidification owing to the extremely low solubility of Fe in Al at room temperature compared with its highly solubility in liquid Al. Numbers of Fe-rich intermetallics have been reported for different Al alloys, e.g., $Al_3Fe$, $Al_6Fe$ and $Al_mFe$ [6-11]. Regarding Al-Si cast alloys, the two most commonly encountered Fe-rich intermetallics are generally Chinese script $Al_8Fe_2Si$ (α-Fe) and platelet $Al_5FeSi$ (β-Fe) [12].

Owing to the platelet morphology of β-Fe, they can block metal feeding and thus generate many porosities during solidification [13], therefore make alloys more easily fractured under tensile loads [2, 4, 14] and then lead to the decreased ductility and strength [15]. Chinese script Fe-rich intermetallics are less detrimental to mechanical properties [2, 16]. Therefore, the modification of Fe-rich intermetallics from platelet into Chinese script has attracted much attention in Al-Si cast alloys. Rapid solidification [17-18] and melt superheating [19] can promote the formation of Chinese-script Fe-rich intermetallics instead of platelet ones during solidification. However, these methods are limited in the practical application as they can promote hydrogen absorption and increase manufacturing costs. Up to date, chemical modifications of Fe-rich intermetallics are more promising and popular. Some alloying elements such as Cr [20], Co [21] have been reported to be effective either in hindering the platelet β-Fe growth or transferring the morphology of Fe-rich intermetallics from platelet into Chinese script. In the foundry practice, Mn is one of the most economical and effective elements to neutralize the detrimental effects of Fe [2]. However, there are still controversies on the influence of Mn on Fe-rich intermetallics. For instance, some researchers [22-23] have stated that an Mn/Fe ratio of 0.5 is sufficient to fully modify the β-$Al_5FeSi$ phase, whereas Seifeddine and Johansson et al. [24] reported that even for an Mn:Fe ratio of 2:1, the β-$Al_5FeSi$ phase cannot be completely replaced by the α-$Al_{15}(FeMn)_3Si_2$ Chinese script phase. One of the likely reasons can be the different variants of Fe-rich intermetallics, in particular, the platelet β-$Al_5FeSi$ with its various chemical compositions and morphology formed at different temperatures depending on Fe contents. However, the research works on the evolution of Fe-rich intermetallics with Fe contents in Al-Si-Cu cast alloys in terms of formation temperature, phase type and morphology during solidification are quite limited, and sometimes even contradicting opinions in the literature exists [25, 26].

Molybdenum (Mo) is a transition metal of the sixth group in the periodic table, which is widely used as an alloying element for high-strength steels and stainless steels. However, it has not received much attention with regard to Al alloys, and only few applications in the rapid-solidification powder metallurgy for elevated temperature uses

have occurred [27]. Recently, it has been applied in Al-Si 356 cast alloys to promote Mo-containing dispersoids [28-29], in which Mo was reported to suppress the formation of β-Fe intermetallics. However, systematical research on the phase selection and precipitation behavior of Fe-rich intermetallics with various Mo additions in Al-Si cast alloys is scarce.

In the present study, the precipitation behavior of Fe-rich intermetallics in Al–Si 319 alloys with two Fe contents (0.3% and 0.7%) was thoroughly studied. The influence of the Mo content on the phase competition of Fe-rich intermetallics was systematically investigated. Furthermore, the effect of the combined addition of Mn and Mo on the different Fe-rich intermetallics was studied and discussed.

## 2. Materials and Methods

The experimental Al-Si-Cu 319 cast alloys were produced with commercially pure Al (99.7%), pure Mg (99.9%), Al-50%Cu, Al-50%Si, Al-25%Fe, Al-25%Mn, and Al-10%Mo master alloys. The chemical composition of experimental alloys analyzed by optical emission spectrometry is listed in Table 1. All alloy compositions in this study are in wt.%, unless otherwise indicated.

In order to investigate the formation and evolution of iron-rich intermetallics in Al-Si-Cu 319 cast alloys at various Fe contents, cast samples with two different Fe contents were produced: the typical industrial Fe content (0.7 %) as well as the general content of Fe in aluminum alloys (0.3 %). The standard Mn content in 319 cast alloys (0.25 %) was used in present work while the maximum content of Mo at 0.4 wt.% with reasonable gap (0, 0.15% and 0.3%) was added due to the solubility of Mo in aluminum (~0.4 wt.%) to investigate the influence of individual Mo addition and combined additions of Mn and Mo on the phase precipitation of Fe-rich intermetallics.

For the casting, the materials were melted at 760 °C in a graphite crucible using an electrical resistance furnace. High-purity argon gas was used to minimize the hydrogen content in the melt for 15 min. Afterward, the liquid metal was poured into a permanent mold preheated at 250 °C to cast ingots. Thermal analysis (TA) was conducted with a small crucible filled with liquid metal to record the temperature changes during solidification. In some cases, the small crucible was quenched in water at a selected temperature to verify the formation of various Fe-rich intermetallics.

Table 1 Chemical composition of the experimental alloys

| Alloy | Elements (wt. %) | | | | | | | |
|---|---|---|---|---|---|---|---|---|
| | Si | Cu | Mg | Ti | **Fe** | **Mo** | **Mn** | Al |
| L0 | 5.35 | 3.19 | 0.08 | 0.10 | **0.28** | 0 | 0 | Bal |
| LM1 | 6.00 | 3.36 | 0.09 | 0.16 | **0.32** | **0.19** | 0 | Bal |
| LM2 | 6.02 | 3.42 | 0.09 | 0.14 | **0.31** | **0.32** | 0 | Bal |
| LM3 | 5.92 | 3.44 | 0.09 | 0.13 | **0.31** | **0.37** | 0 | Bal |
| H0 | 5.81 | 3.28 | 0.10 | 0.11 | **0.64** | 0 | 0 | Bal |
| HM1 | 6.00 | 3.35 | 0.09 | 0.12 | **0.67** | **0.18** | 0 | Bal |
| HM2 | 5.94 | 3.32 | 0.07 | 0.10 | **0.65** | **0.30** | 0 | Bal |
| HM3 | 5.89 | 3.41 | 0.11 | 0.10 | **0.70** | **0.41** | 0 | Bal |
| Mn1 | 6.18 | 3.4 | 0.09 | 0.12 | **0.66** | 0 | **0.25** | Bal |
| Mn2 | 6.04 | 3.39 | 0.10 | 0.11 | **0.68** | **0.15** | **0.25** | Bal |
| Mn3 | 6.18 | 3.46 | 0.09 | 0.14 | **0.69** | **0.30** | **0.26** | Bal |
| Mn4 | 6.02 | 3.52 | 0.09 | 0.17 | **0.66** | **0.41** | **0.24** | Bal |

The specimens for the microstructural characterization were cut from the cast ingots and prepared with the traditional metallographic procedure. The evolution of the microstructures was examined and quantified using an optical microscope equipped with a Clemex image analyzer. For each sample, 50 fields were measured over the entire sample surface, and the area percentages of various Fe-rich intermetallics were obtained from the average measurement values. A scanning electron microscope (SEM; JEOL JSM-6480LV) equipped with an energy-dispersive X-ray spectroscope (EDS) and electron backscatter diffraction (EBSD) system was used to characterize the various Fe-rich intermetallics in the experimental alloys. Moreover, a differential scanning calorimetry (DSC; Perkin Elmer DSC 8000) was employed to identify and confirm the precipitation as well as the evolution of the Fe-rich intermetallics during the solidification with a heating rate of 10 °C /min.

## 3. Results and Discussion

### 3.1 Precipitation of Fe-rich Intermetallics in experimental alloys

The typical microstructure of the experimental alloys consists of α-Al dendrites, eutectic Si, θ-$Al_2Cu$ intermetallic, as well as various Fe-rich intermetallics with different morphologies. The typical Fe-rich intermetallics in this study are shown in Fig. 1 (indicated by white arrows), and they can be first differentiated by two morphologies: a platelet morphology and a Chinese script shape. The Fe-rich intermetallics in Alloys H0 and L0 (Fig. 1a and 1b) have the platelet morphology, whereas they display the Chinese script shape in Alloy Mn1, LM2 and Mn3(Fig. 1c–1e). The SEM-EDS analysis was applied to further distinguish these intermetallics (EDS results shows the average from

values of at least ten similar intermetallics in the same alloy). It can be found the platelet Fe-rich intermetallics ("A" in Alloy H0 and "B" in Alloy L0) have the similar Si:Fe ratio, which is close to 1. Therefore, they are identified as β-$Al_5FeSi$ (β-Fe) according to their platelet morphology and EDS results, which is in good agreement with the literature [30]. On the other hand, the Chinese script intermetallics ("C", "D" and "E") contain less Si and Fe but more Mn or/and Mo depending on the alloys. However, their (Fe+X(Mn, Mo)):Si ratio is similar to 1.5:1 (Table 2), indicating the similarity to the $Al_{15}(FeX)_3Si_2$ intermetallic, which is reported as α-Fe in literature [5].

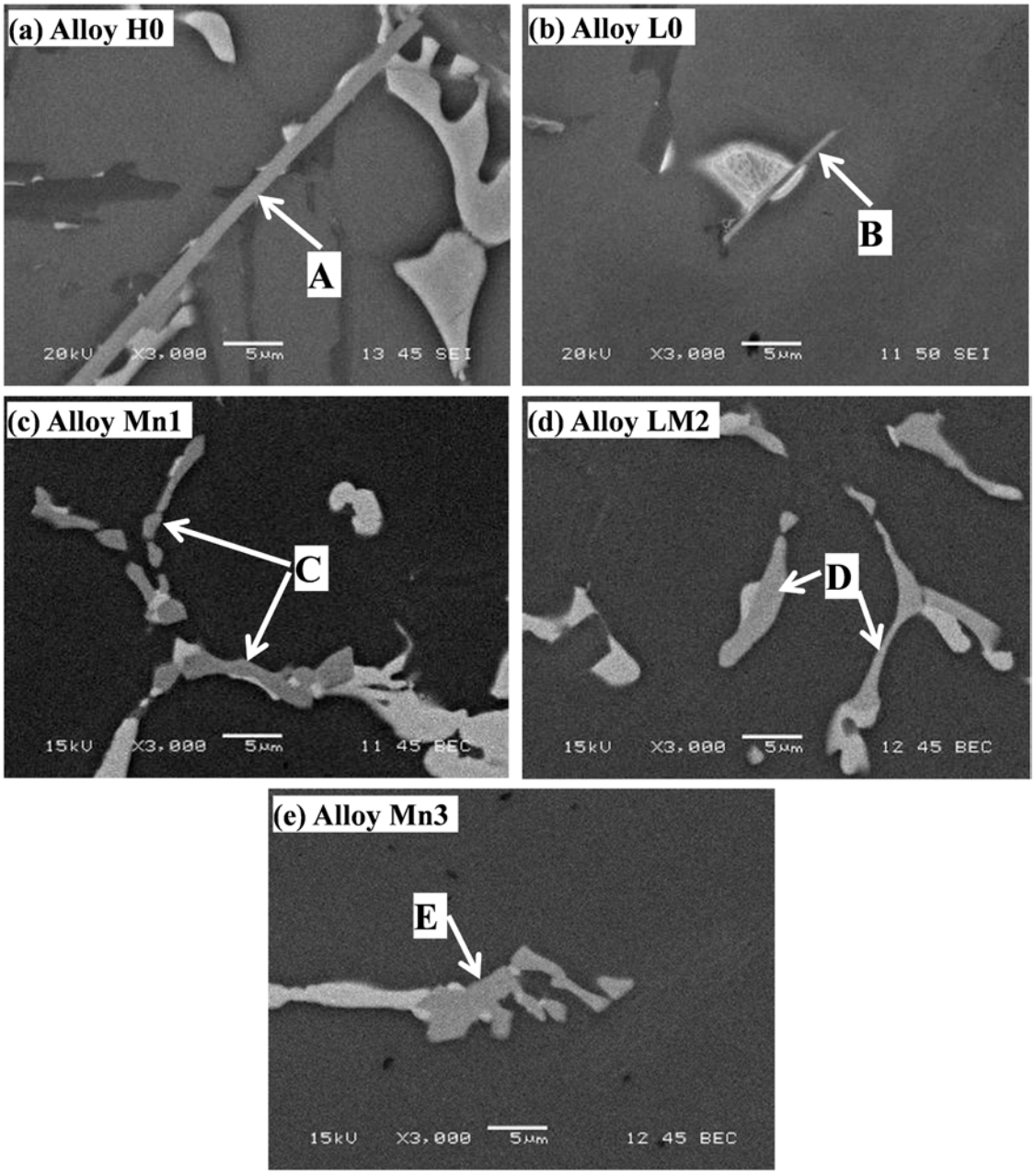

Fig. 1 Typical Fe-rich intermetallics (indicated by arrows) in:
(a) Alloy H0, (b) Alloy L0, (c) Alloy Mn1, (d) Alloy LM2, and (e) Alloy Mn3.

Table 2 SEM-EDS results of the Fe-rich intermetallics shown in Fig. 1

| Morphology | Phase | Elements (at. pct.) | | | | |
|---|---|---|---|---|---|---|
| | | Al | Si | Fe | Mn | Mo |
| Platelet | A | 68.8±3.9 | 17.7±2.4 | 13.5±2.1 | N/A | N/A |
| | B | 67.0±2.6 | 17.7±1.4 | 15.0±0.9 | N/A | N/A |
| Chinese Script | C | 68.4±1.0 | 12.4±1.0 | 10.8±0.9 | 8.4±1.3 | N/A |
| | D | 69.1±3.1 | 12.9±1.7 | 10.2±1.4 | N/A | 7.8±1.3 |
| | E | 68.2±4.8 | 12.4±5.1 | 10.5±1.5 | 4.2±1.0 | 5.1±1.0 |

As shown in Fig. 1a and 1b, even with a similar platelet morphology, the disparities in size of platelet β-Fe are great; in particular, the length, which can reach 100 μm in Fig. 1a for Alloy H0 with high Fe content (0.7%), whereas it generally exhibits less than 30 μm in Fig. 1b for Alloy L0 with low Fe content (0.3%). The large difference in the size regarding β-$Al_5FeSi$ in Alloys L0 and H0 suggests that they might be precipitated at different stages of the solidification process. Therefore, a TA was conducted for Alloys L0 and H0 and the results are shown in Fig. 2 together with the corresponding microstructure from the interrupted water quench test at 570 °C and 540°C. As shown in Fig. 2a and 2b, Peaks 1, 2, and 3 stand for the precipitations of α-Al dendrite, eutectic Si, and θ-$Al_2Cu$ intermetallic, respectively, while Peaks 4 and 5 represent the precipitation of Fe-rich intermetallics [30]. In order to determine the corresponding phases of Peaks 4 and 5, interrupted water quench tests were performed at two distinctive temperatures: 570 °C (after Peak 4; dotted line I) and 540 °C (after Peak 5; dotted line II). The corresponding microstructures are shown in Fig. 2c–2f. Evidently, no Fe-rich phase can be observed in Alloy L0 at 570 °C (Fig. 2c), whereas several long platelet β-$Al_5FeSi$ phases appear in Alloy H0 (indicated by black arrow in Fig. 2d), which implies that Peak 4 corresponds to the precipitation of the long platelet β-$Al_5FeSi$ phase. Since the formation temperature of this kind β-$Al_5FeSi$ is at approximately 580 °C, which is higher than that for eutectic Si (Peak 2 in Fig. 2b), these long platelet β-$Al_5FeSi$ were then designated as P-β-Fe (pre-eutectic β-$Al_5FeSi$) in this study. For 540 °C (dotted line II), short and thin β-$Al_5FeSi$ phases appear in the quenched microstructure in both L0 and H0 alloys (as indicated by white arrows in Fig. 2e and 2f) and they were designated as E-β-Fe (eutectic β-$Al_5FeSi$) due to their lower formation temperature. Obviously, the size of the P-β-Fe phase is much

bigger than that of E-β-Fe. The smaller size of the E-β-Fe phase in Alloy L0 can be attributed to its phase precipitation at the lower temperature (approximately 560 °C). It should also be noted that, only a minor peak can be observed for E-β-Fe in Alloy H0, which can be attributed to the lower volume fraction of E-β-Fe compared to that of E-β-Fe in Alloy L0.

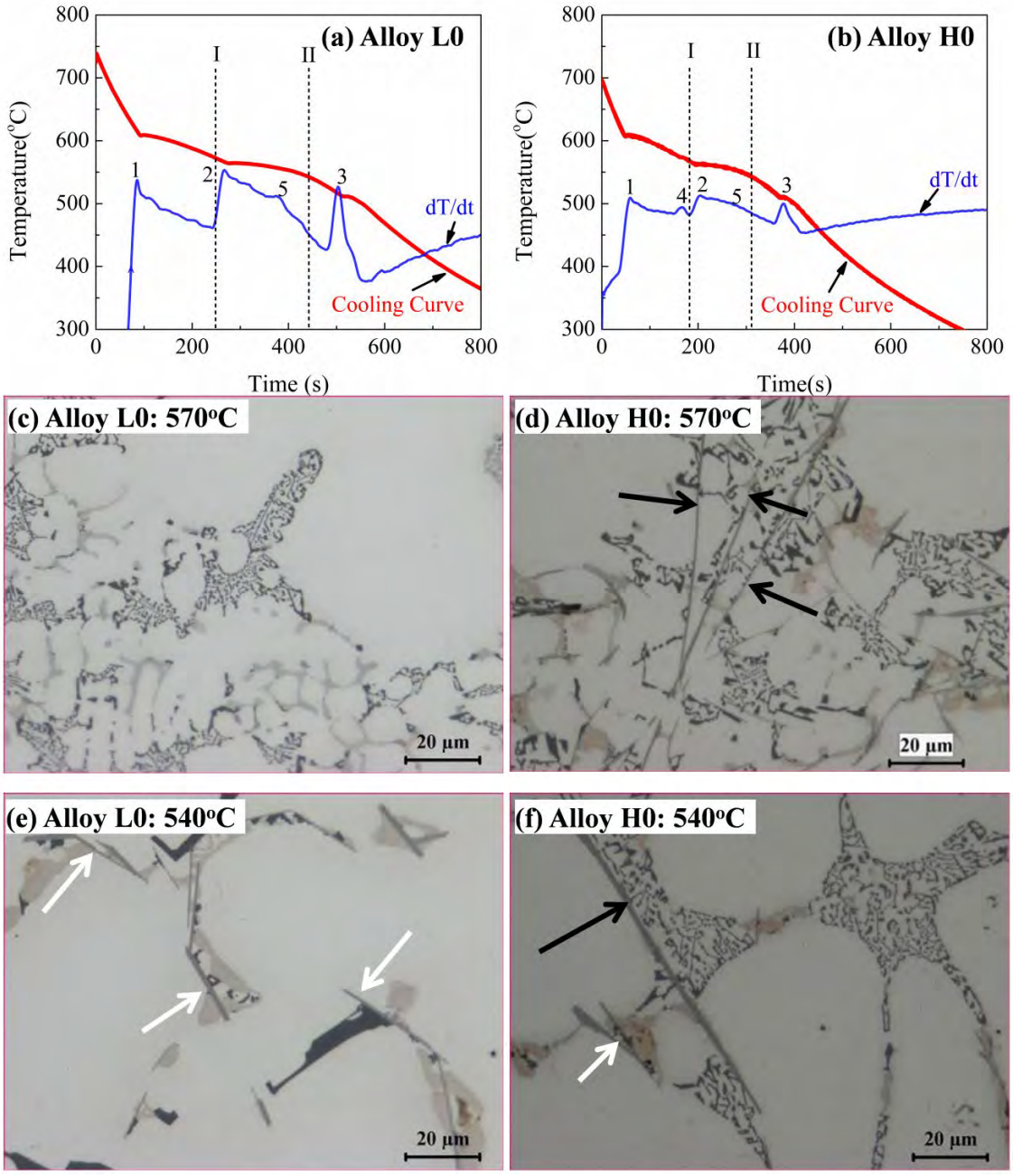


Fig. 2 TA curves of (a) Alloy L0 and (b) Alloy H0 as well as microstructure after interrupted water quench at: (c) 570°C and (e) 540°C of Alloy L0; (d) 570°C and (f) 540°C of Alloy H0

(black and white arrows indicate P-β-Fe and E-β-Fe, respectively).

As shown in Table 2, the Chinese script Fe-rich intermetallics in Fig. 1c-1e are indicated as α-Fe in alloys with Mn and Mo additions based on their chemical compositions. However, different Chinese script α-Fe with similar chemical composition were reported in Al-Si-Cu alloys yet with different crystal structures, e.g., monoclinic $Al_9Fe_2Si$ [31] and cubic $Al_{15}(FeMn)_3Si_2$ [5]. Therefore, for more accurate phase identification, EBSD was applied to further investigate these Chinese script intermetallics by comparing simulated EBSD pattern of individual Chinese script Fe-rich intermetallics with standard EBSD patterns of corresponding phases and their mean angular deviation (MAD) value. As an example, Fig. 3 shows the EBSD pattern and simulated results of the Chinese script phase "E" containing Mn and Mo in Alloy Mn3 (Table 2 and Fig. 1e). It can be found that the pattern matches well with the standard pattern of the $Al_{15}(FeX)_3Si_2$-type crystal structure with the mean angular deviation (MAD) of 0.556, which is lower than the acceptable MAD value of 0.7 for the accurate phase identification [32]. Meanwhile, the average MAD value for the Chinese script phase in Figs. 1c and 1d are both lower than 0.7 (0.340 for "C" and 0.531 for "D"). The different MAD values of Chinese script phase in different alloys can be attributed to the lattice distortion due to the replacement between Fe, Mn and Mo atoms. Hence, all the Chinese script Fe-rich intermetallics in the present work were identified as cubic $Al_{15}(FeX)_3Si_2$ from combined results of EDS and EBSD. These Chinese script Fe-rich intermetallics were all designated indiscriminately as α-Fe though they might have slight variation in their chemical compositions due to the different Mn and Mo additions in experimental alloys.

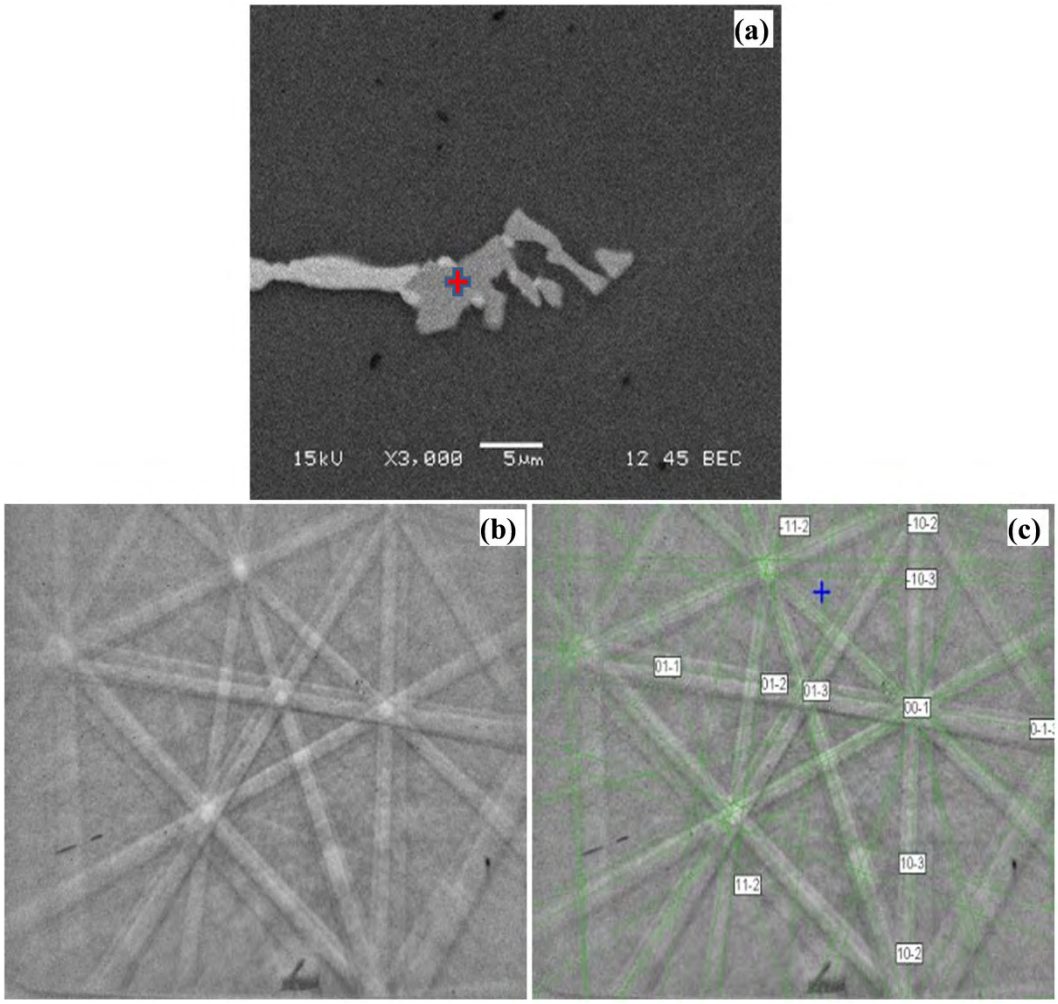


Fig. 3 Chinese Script Fe-rich intermetallic in Alloy Mn3 (a) and its EBSD pattern (b) as well as the simulation results (c)

Fig. 4 shows the TA curves of Alloys LM3 and HM3 together with the corresponding microstructure from the interrupted water quench test at 580 °C. Compared with H0 in Fig. 3, a new peak occurs (Peak 6) at 590 °C for Alloy LM3 (Fig. 4a) and Alloy HM3 (Fig. 4b). Fig. 4c and 4d present the microstructures from the interrupted water quench test after Peak 6 for 580 °C (indicated by dotted line). Chinese script α-Fe (indicated by black arrows) are the dominant Fe-rich intermetallics in both Alloy LM3 (Fig. 4c) and Alloy HM3 (Fig. 4d), thereby confirming the precipitation of α-Fe at Peak 6. It should also be noted that the peak intensity of Alloy LM3 is lower than that of Alloy HM3, which can be derived from their lower volume fraction in Alloy LM3.

Based on the metallographic observations and results obtained from TA in our work

together with some previous studies [33-34], Table 3 summarizes the various Fe-rich intermetallics formed in the investigated alloys. It can be found that the type of Fe-rich intermetallic strongly dependent on the alloy compositions. For instance, E-β-Fe is present in all alloys except LM3 and Mn4 while P-β-Fe can only exist for alloys with higher Fe contents (0.7%), whereas α-Fe is almost ubiquitous except for Alloy H0.

Table 3 Formation of Fe-rich intermetallics in experimental alloys

| Peak | Phases | Alloys |
|---|---|---|
| 4 | P-β-Fe | H0, HM1, HM2, Mn1, Mn2, Mn3 |
| 5 | E-β-Fe | All alloys except LM3, Mn4 |
| 6 | α-Fe | All alloys except H0 |

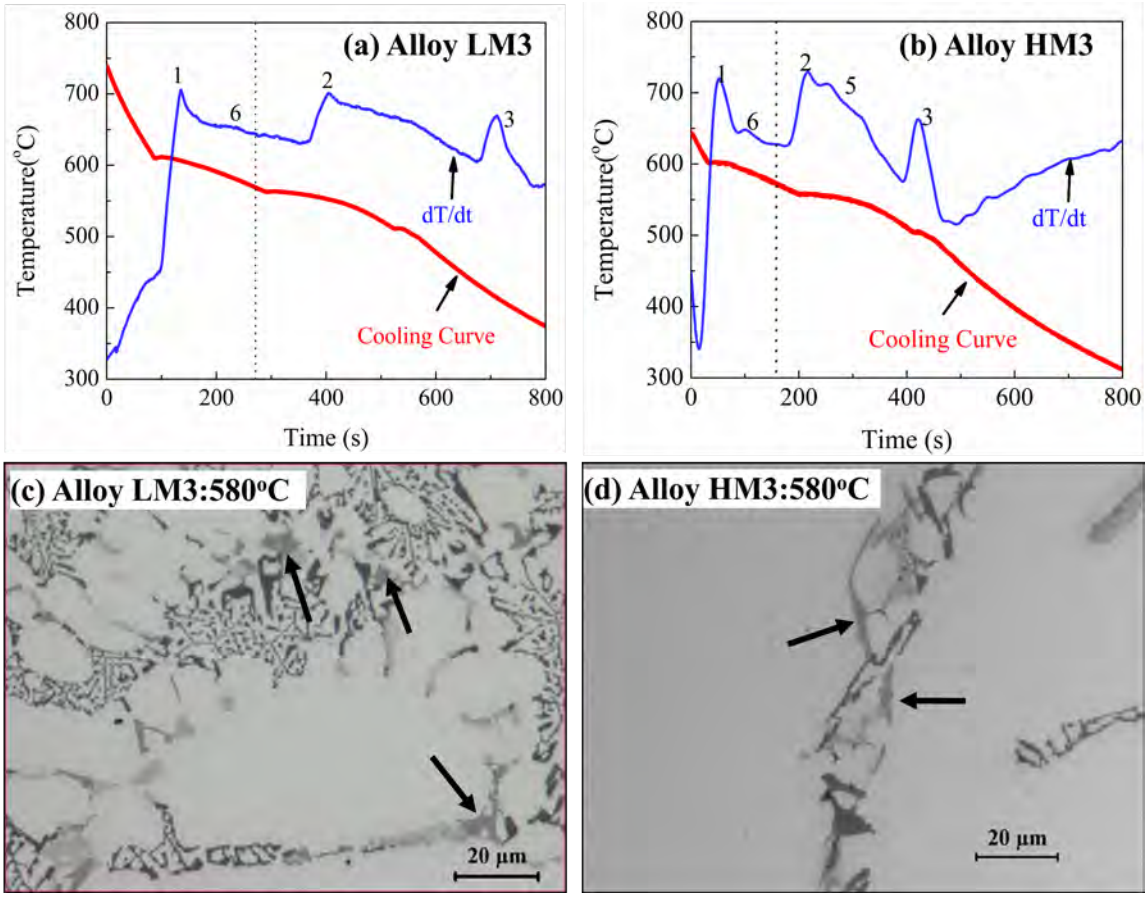


Fig. 4 TA curves of alloys: (a) LM3 and (b) HM3 and microstructure after interrupted water quench at 580 °C of (c) LM3 and (d) HM3 alloys (black arrows indicate α-Fe)

3.2 Evolution of Fe-rich intermetallics with Mo and Mn additions

As shown in Table 3, various Fe-rich intermetallics exist in the different alloys with various combinations of Fe, Mo, and Mn contents. Even for same Fe content, the existing Fe-rich intermetallics can change depending on the Mo contents, thereby indicating a possible preferential phase selection and competition of Fe-rich intermetallics under different chemical compositions. Therefore, alloys with various Mo and Fe contents were examined and the microstructures are presented in Fig. 5.

Regarding the alloys with low Fe content (0.3%), Alloy L0 without Mo (Fig. 5a), considerable numbers of E-β-Fe phases (indicated by white arrow) dominate the microstructure. After only 0.15% Mo addition (Fig. 5b), the E-β-Fe phases partially disappear, as reflected by their smaller sizes and decreasing volumes. It is noteworthy that some α-Fe phases (indicated by thick black arrow) start to form in Alloy LM1 compared to negligible amounts of α-Fe phases in Alloy L0 in Fig. 5a and their volume fraction increases with increasing Mo content. After the addition of 0.37% Mo in Alloy LM3 (Fig. 5c), the amount of the E-β-Fe phase significantly decreases to an almost unnoticeable amount, whereas the amount of the α-Fe phases increases significantly until α-Fe becomes the sole Fe-rich intermetallic in Alloy LM3.

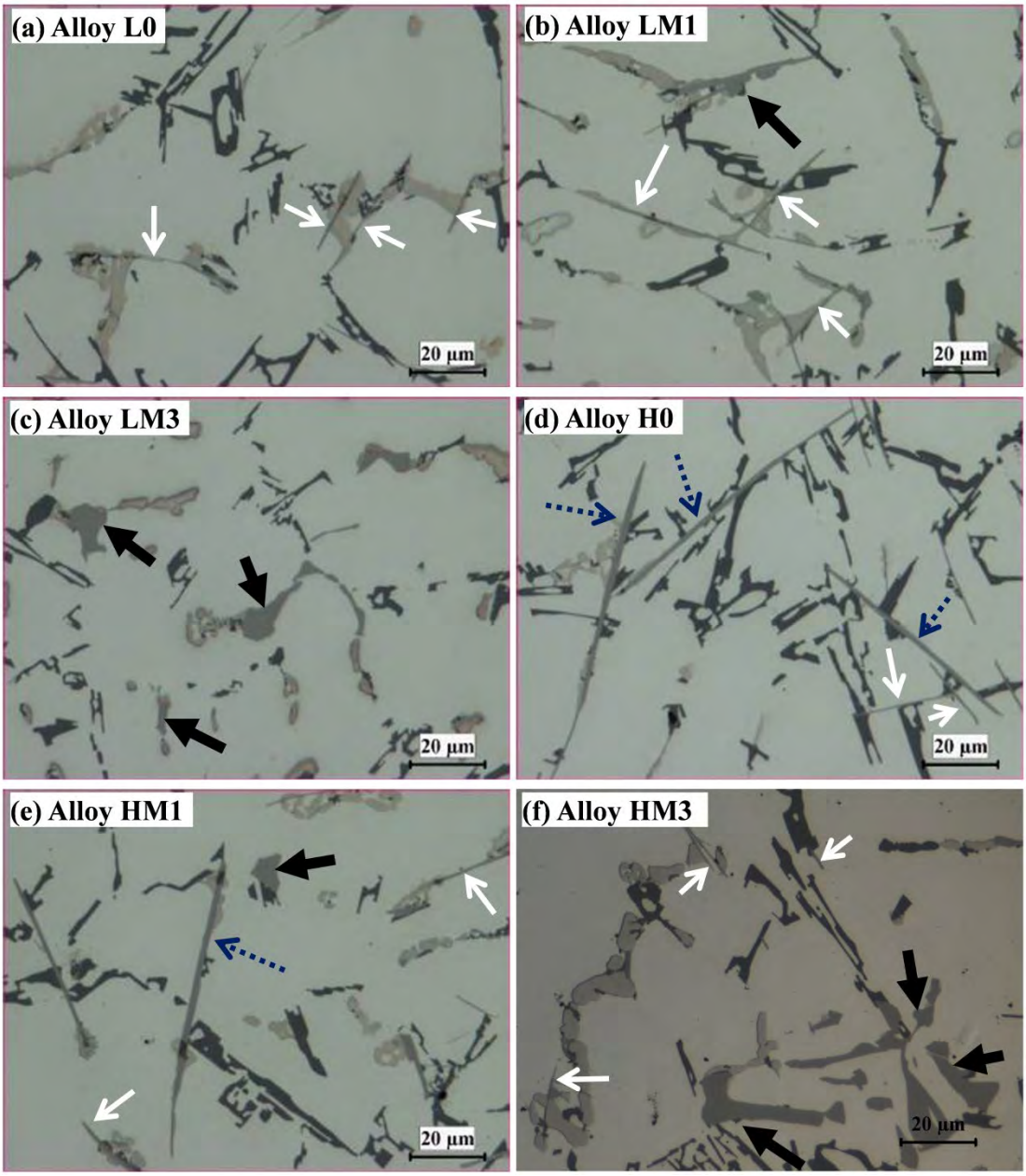


Fig. 5 Optical micrographs showing effect of Mo on microstructure for low-Fe (0.3%) alloys: (a) L0, (b) LM1, and (c) LM3; for high-Fe (0.7%) alloys: (d) H0, (e) HM1, and (f) HM3 (white, blue dotted and black arrows indicate E-β-Fe, P-β-Fe, and α-Fe, respectively)

In Alloy H0 (high Fe content but free of Mo; Fig. 5d), a considerable number of P-β-Fe (indicated by blue dotted arrow) and E-β-Fe phases (indicated by white arrow) coexist. After the addition of 0.15% Mo in Alloy HM1 (Fig. 5e), P-β-Fe was partially suppressed

but a relatively high volume of E-β-Fe can still be observed. Further, for the addition of up to 0.41% Mo (Alloy HM3; Fig. 5f), the volume of the P-β-Fe phase significantly decreases to an approximately unnoticeable volume, whereas E-β-Fe phases are still visible in the microstructure. Besides, α-Fe phase begins to form for an addition of 0.15% Mo (indicated by white arrow) in Fig. 5e and its amount also increases with increasing Mo content (Fig. 5e–5f). Apparently, approximately all E-β-Fe phases are suppressed and microstructure with dominant α-Fe is obtained with a sufficient Mo addition in alloys with lower Fe content (0.3%), such as LM3 in Fig. 5c. For alloys with high Fe content (0.7%), although Mo addition also promotes the formation of Chinese Script α-Fe phases. However, even with 0.41% Mo addition, the E-β-Fe is not completely suppressed, this is likely due to the high-Fe content consume more Mo to suppress the formation of P-β-Fe, leaving limited amount of Mo to further suppress the formation of E-β-Fe. The possible reasons for the phase suppression and selection will be discussed later in this section.

Fig. 6 shows the quantified analysis results of area fractions of various Fe-rich intermetallics. Generally, the total area fractions of the Fe-rich intermetallics are similar in alloys with same Fe content while the total area fractions increase with increasing Fe content. As shown in Fig. 6a and 6b, the total area fractions of Fe-rich intermetallics in alloys with low Fe content (0.3%) remain at approximately 1.15% (Fig. 6a) and increase to approximately 2.05% in alloys with high Fe content (0.7%) (Fig. 6b). For the individual Fe-rich intermetallics, the area fraction of α-Fe increases with increasing Mo addition while the evolutions of P-β-Fe and E-β-Fe are different in both low Fe and high Fe alloys. As in low Fe alloy (Fig. 6a), the proportion of α-Fe in the total intermetallic fraction increases from 0 in Alloy L0 to 20.7% and 41.9% in alloys LM1 and LM2, respectively, until it reaches 100% in Alloy LM3 without E-β-Fe. Regarding the alloys with high Fe content (Fig. 6b), the proportion of α-Fe in the total intermetallic fraction increases from 0 (Alloy H0) to 15.8% (Alloy HM1), 57.9% (Alloy HM2), and 78.9% (Alloy HM3) with increasing Mo additions. However, a moderate amount of E-β-Fe still remains. By contrast, the P-β-Fe phase completely disappears for the maximum Mo addition of 0.41% (Fig. 6b).

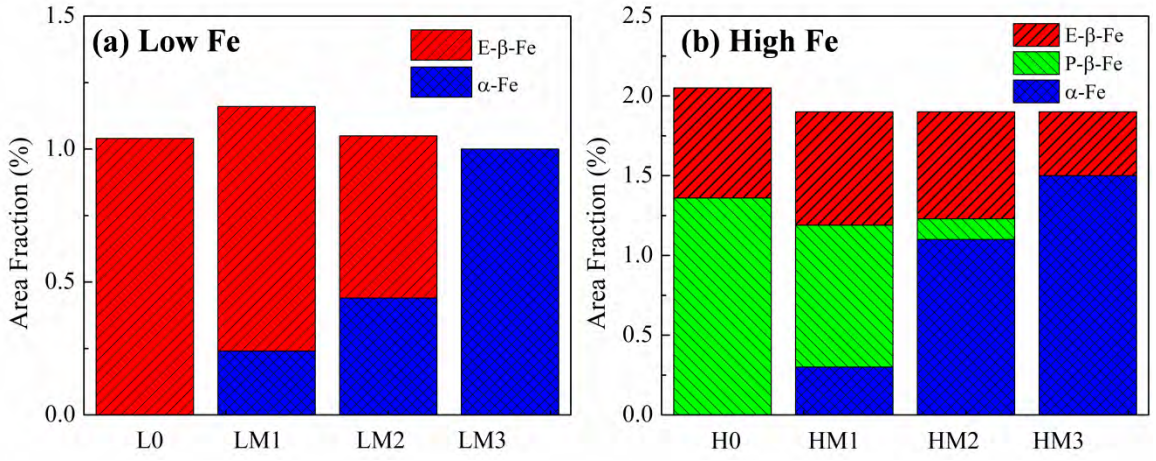


Fig. 6 Area fractions of α-Fe, P-β-Fe, and E-β-Fe for different Mo additions in (a) Low Fe alloy, (b) High Fe alloy.

As shown in Figs. 5 and 6, the Mo addition can significantly promote the formation of Chinese script α-Fe while inhibit the precipitation of E-β-Fe at low Fe content (0.3%) and P-β-Fe at high Fe content (0.7%). It is reported that the Mn addition can increase the formation temperature of α-Fe but decrease that of β-Fe in Al-Cu 206 cast alloys [35], explaining the promoting effect of Mn on Chinese script Fe-rich intermetallics. Therefore, it is also to be expected that Mo addition can have similar influence on the formation temperature of various Fe-rich intermetallics in our study, leading to evolution of Fe-rich intermetallics shown in Figs. 5 and 6. Therefore, the DSC was employed in present work in order to investigate the effect of the Mo addition on the evolution of various Fe-rich intermetallics and results are shown in Fig. 7. Regarding the alloys with low Fe content (0.3%) in Fig. 7a, Peak 5 (corresponding to E-β-Fe) significantly decreases with increasing Mo addition and it nearly disappears for 0.37% Mo addition in Alloy LM3. This is in a good agreement with the area fraction results(Fig. 6a) and study [13]. Fig. 7c presents the enlarged zone of Peak 5 in Fig. 7a. The decreasing peak area with increasing Mo content confirms the decreasing volume fraction of E-β-Fe. Moreover, the formation temperature of E-β-Fe shifts to lower temperature with increasing Mo addition, thereby indicating the suppression of E-β-Fe formation via Mo addition.

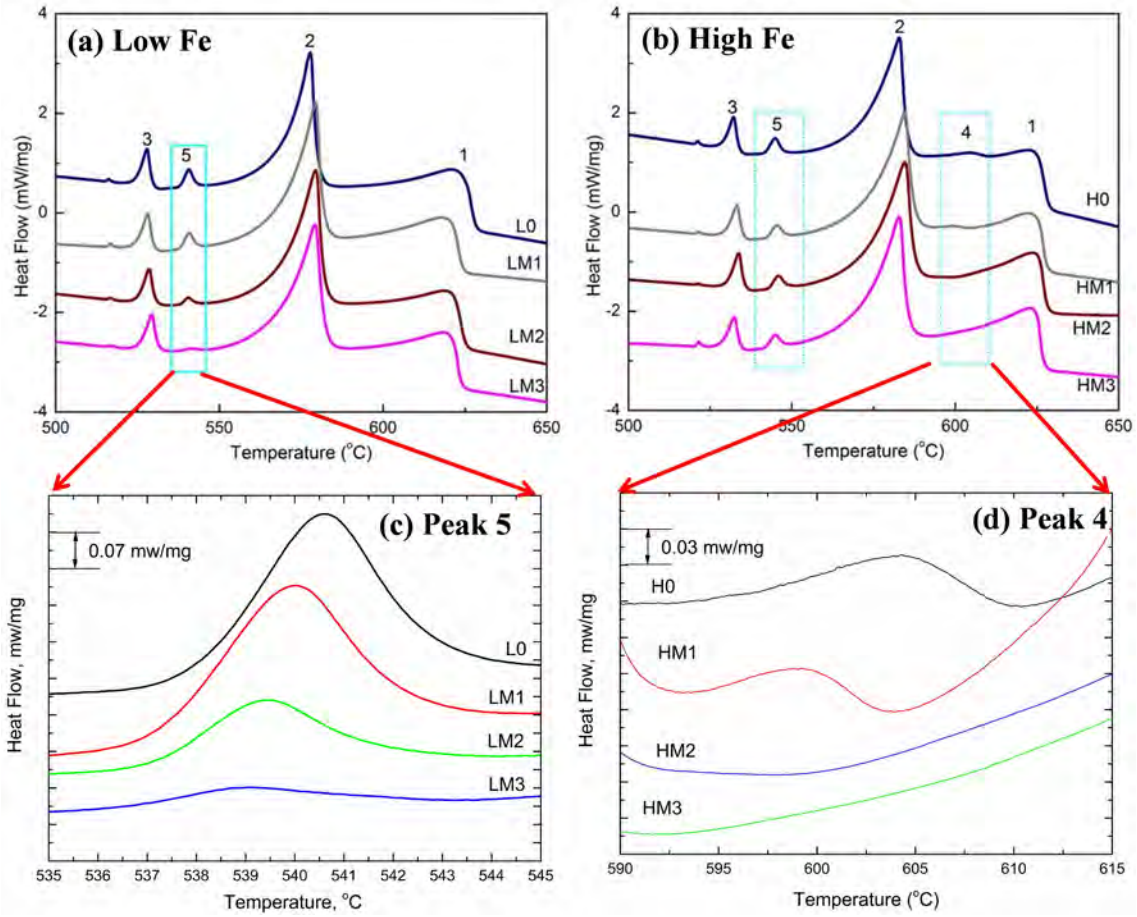


Fig. 7 DSC heating curves of (a) low-Fe alloys, (b) high-Fe alloys and (c) enlarged zone 5 in (a) while (d) enlarged zone 4 in (b)

For alloys with high Fe content (0.7%) in Fig. 7b, Peak 4 (corresponding to P-β-Fe) decreases with increasing Mo additions, confirming the hindering effect of Mo on the formation of P-β-Fe intermetallics, whereas Peak 5 (corresponding to E-β-Fe) displays no significant changes even for 0.41% Mo addition in Alloy HM3. Fig. 7d shows the enlarged Peak 4 (P-β-Fe) in high Fe content(0.7%) alloys, it is evident that the peak intensity and precipitation temperature of the P-β-Fe phases decrease with increasing Mo contents, confirming that the P-β-Fe precipitation is also suppressed by the Mo addition. Thus, the peak intensity and formation temperature of both E-β-Fe in low Fe content and P-β-Fe in high Fe content decrease with increasing Mo addition, confirming the hindering effect of Mo on the formation of β-Fe phase. The disappearance of the platelet E-β-Fe/P-β-Fe phases with increasing Mo addition can be attributed to their different formation temperatures during solidification. As shown in Figs. 3 and 4, the formation temperature increases from E-β-Fe, P-β-Fe, to α-Fe. When Mo is added, Mo first interacts with Al, Fe,

and Si to precipitate α-Fe before the precipitation of P-β-Fe and E-β-Fe, leaving less Fe available for the formation of P-β-Fe/E-β-Fe and thus decreasing their volume fractions.

Owing to the limited solubility of Mo in Al alloys [35], a further increase in the Mo addition results in the formation of an primary Al–Mo intermetallic component during solidification and limited its further influence on the Fe-rich intermetallics. On the other hand, Mn was reported to be effective in neutralizing the platelet β-Fe, especially the eutectic β-Fe [13]. Hence, the combined addition of Mn and Mo was also investigated for the alloys with high Fe content(0.7%) to completely suppress the formation of platelet β-Fe phases and the evolutions of the microstructures are presented in Fig. 8.

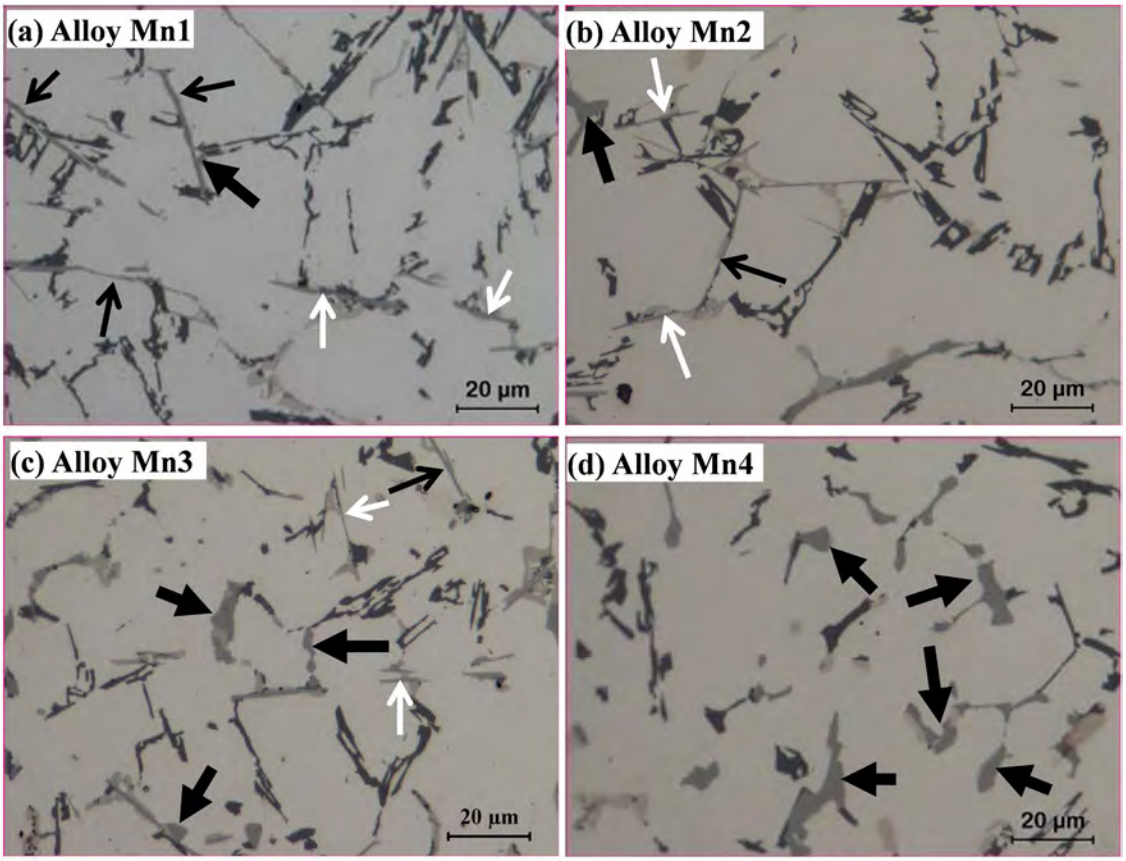


Fig. 8 Optical images of alloys: (a) Mn1, (b) Mn2, (c) Mn3, and (d) Mn4 (white, black, and thick black arrows indicate E-β-Fe, P-β-Fe, and α-Fe, respectively)

In Alloy Mn1 (Fig. 8a), a small amount of α-Fe (indicated by thick black arrows) co-exist with P-β-Fe ( thin black arrows) and E-β-Fe (white arrows), indicating the positive effect of Mn on α-Fe intermetallics compared with Alloy H0 with only P-β-Fe and E-β-Fe (Fig. 5d). For the combined addition of Mn and Mo (Fig. 8b and c), the area fraction of

both P-β-Fe and E-β-Fe decreases while that of α-Fe increases; In particular, in Alloy Mn4 with 0.41% Mo and 0.24% Mn, both P-β-Fe and E-β-Fe disappear completely, leaving α-Fe as the sole Fe-rich intermetallic (Fig. 8d), indicating the complete suppression of β-Fe due to the combined Mn and Mo additions.

The evolutions of the area fractions of α-Fe, P-β-Fe, and E-β-Fe intermetallics in the alloys containing Mn and Mo are presented in Fig. 9. With increasing Mo addition in the presence of Mn, area fraction of both P-β-Fe and E-β-Fe decreases, while that of α-Fe increases significantly. For the combined addition of 0.24% Mn and 0.41% Mo (Alloy Mn4), β-Fe is completely suppressed, and a unique α-Fe dominated microstructure is achieved in the high Fe content alloys.

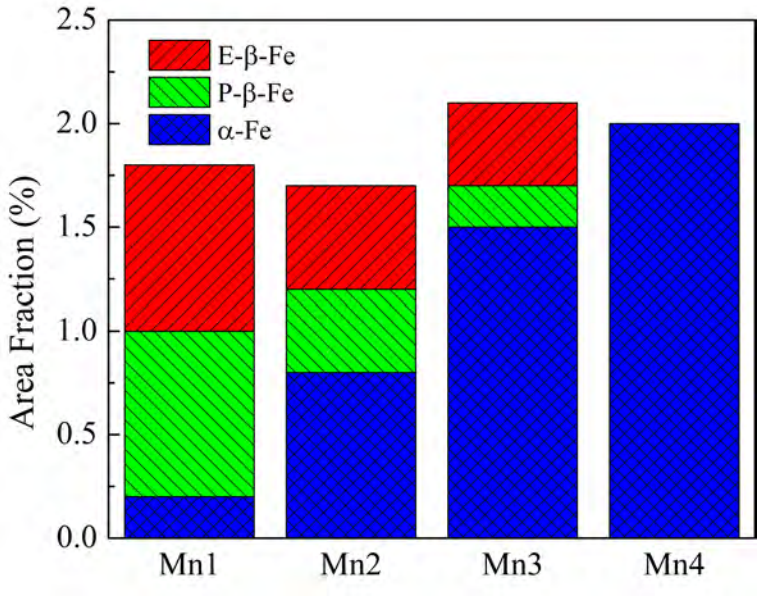


Fig. 9 Area fractions of α-Fe, P-β-Fe, and E-β-Fe in experimental alloys

According to the evolution of Fe-rich intermetallics with equal Fe contents presented in Fig. 9 and 6b, it can be inferred that Mo exhibits a stronger effect than Mn on the promotion of α-Fe precipitation. For instance, there is an 0.2% area fraction of α-Fe in Alloy Mn1 (0.25% Mn), whereas the area fraction of α-Fe reaches 1.1% in Alloy HM2 (0.3% Mo). Al-Si-Cu 319 cast alloy is generally secondary alloy with higher Fe content, the necessity to efficiently reduce Fe content is often prioritized in industrial practice. Thus the effect of Mn and Mo in suppressing P-β-Fe and promoting α–Fe is compared, and the correlation of Mo/Mn contents and area fractions of the P-β-Fe/α-Fe phases was established on the calculated area fractions from Figs. 6 and 9 in high Fe content (0.7%)

alloys, and presented in Fig. 10.

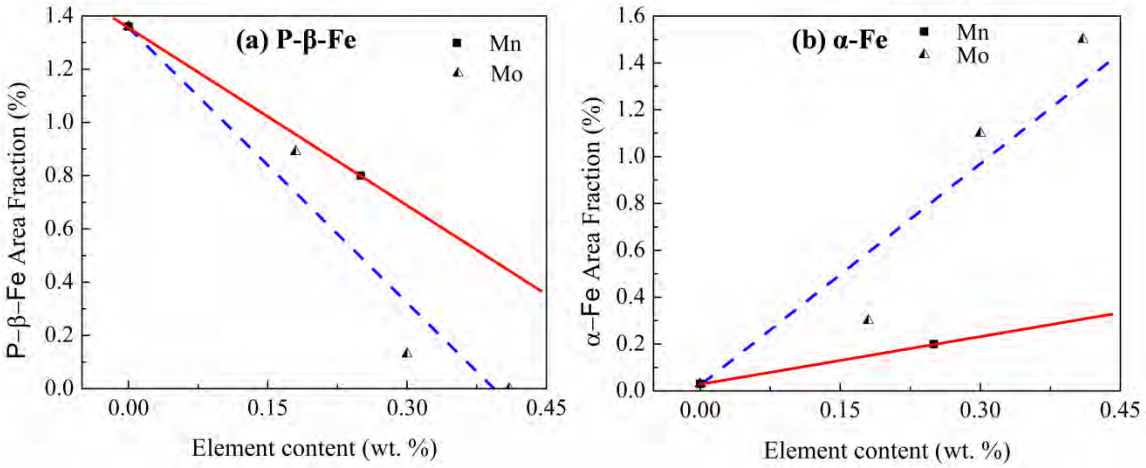


Fig.10 Correlation between Mo and Mn contents with area fractions of (a) P-β-Fe and (b) α-Fe in alloys with high Fe contents (0.7%)

As shown in Fig. 10a, the relative area fraction of the P-β-Fe phase decreases with increasing Mo and Mn additions. However, the decreasing rate due to the Mo addition is much larger than that caused by Mn, thereby indicating a stronger suppressing influence of Mo on P-β-Fe. Similarly, as presented in Fig. 10b, α-Fe generally increases with increasing Mo and Mn contents but the slope due to the Mo addition is much larger than that due to Mn, confirming the stronger effect of Mo on the promotion of α-Fe formation. Therefore, Mo can be more efficient than Mn on suppressing platelet β-Fe and promoting α-Fe from this point of view. However, the solubility of Mo in Al is relatively lower compared with Mn [36]. Thus, combined addition of Mo and Mn is recommended in order to obtain the complete suppression of platelet Fe-rich intermetallics in Al-Si-Cu 319 cast alloys, especially for high Fe contents in industrial applications.

## 4. Conclusions

The formation of Fe-rich intermetallics in Al-Si-Cu 319 cast alloys with various Fe, Mo, and Mn contents was studied in the present work with the following conclusions:

(1) Two types of platelet Fe-rich intermetallics, defined as eutectic and pre-eutectic β-Fe, and one type of α-Fe can precipitate depending on the Fe, Mo, and Mn contents. Without the Mn/Mo additions, only eutectic β-Fe form in the low-Fe alloys (0.3%), whereas pre-eutectic and eutectic β-Fe coexist in the high-Fe alloys (0.7%).

(2) The addition of Mo can strongly promote the formation of α-Fe and suppress the

precipitation of β-Fe in both low-Fe and high-Fe alloy. However, the effect of Mo on the suppression of β-Fe is greatly related to the Fe contents. In low-Fe alloys, the addition of 0.37% Mo can completely suppress eutectic β-Fe. While, only pre-eutectic β-Fe can be reduced with increasing Mo content, leaving the eutectic β-Fe intermetallics almost unchanged in high-Fe alloys.

(3) Both pre-eutectic β-Fe and eutectic β-Fe can be completely suppressed, and a unique α-Fe microstructure can be achieved with a combined addition of Mn (0.24%) and Mo (0.41%) in high-Fe alloys.

(4) Compared with Mn, Mo exhibits a stronger effect in promoting α-Fe precipitation. The combined addition of Mn and Mo can achieve a better modification of both pre-eutectic β-Fe and eutectic β-Fe intermetallics in industrial 319 cast alloys.

## Acknowledgement

The authors would like to acknowledge the financial support from the Natural Sciences and Engineering Research Council of Canada (NSERC) and Rio Tinto Aluminum through the NSERC Industry Research Chair in the Metallurgy of Aluminum Transformation at University of Quebec at Chicoutimi.

## References

1. F. J. Tavitas-Medrano, A. M. A. Mohamed, J. E. Gruzleski, F. H. Samuel and H. W. Doty, *Journal of Materials Science* 2010, vol. 45, pp. 641-651.

2. Mousa Javidani and Daniel Larouche, *Int. Mater. Rev.* 2014, vol. 59, pp. 132-158.

3. B.P. Bhardwaj: *The Complete Book on Production of Automobile Components & Allied Products*. (2014), pp. 171-172.

4. PN Crepeau, *Transactions of the American Foundrymen's Society* 1995, vol. 103, pp. 361-366.

5. N.A. Belov, A.A. Aksenov and D.G. Eskin: *Iron in Aluminium Alloys: Impurity and Alloying Element*. (Taylor & Francis, 2002), pp. 240-241.

6. Nataliya Krendelsberger, Franz Weitzer and Julius C. Schuster, *Metall and Mat Trans A* 2007, vol. 38, pp. 1681-1691.

7. S. P. Gupta, *Materials Characterization* 2002, vol. 49, pp. 269-291.

8. T. Maitra and S. P. Gupta, *Materials Characterization* 2002, vol. 49, pp. 293-311.

9. N. Krendelsberger, F. Weitzer and J. C. Schuster, *Metallurgical and Materials Transactions A: Physical Metallurgy and Materials Science* 2007, vol. 38, pp. 1681-1691.

10. K. Liu, X. Cao and X.-G. Chen, *Metall and Mat Trans A* 2013, vol. 44, pp. 682-695.

11. K. Liu, X. Cao and X.-G. Chen, *Metall and Mat Trans A* 2011, vol. 42, pp. 2004-2016.
12. Nikolay A Belov, Dmitry G Eskin and Andrey A Aksenov: *Multicomponent phase diagrams: applications for commercial aluminum alloys*. (Elsevier, 2005), pp. 20-46.
13. J. Y. Hwang, H. W. Doty and M. J. Kaufman, *Materials Science and Engineering: A* 2008, vol. 488, pp. 496-504.
14. J. A. Taylor, G. B. Schaffer and D. H. StJohn, *Metall and Mat Trans A* 1999, vol. 30, pp. 1657-1662.
15. John A Taylor, In *35th Australian Foundry Institute National Conference*, (Australian Foundry Institute (AFI): 2004), pp 148-157.
16. K. Liu, X. Cao and X.-G. Chen, *Metall and Mat Trans A* 2014, vol. 45, pp. 2498-2507.
17. A. Verma, S. Kumar, P. S. Grant and K. A. Q. O'Reilly, *Journal of Alloys and Compounds* 2013, vol. 555, pp. 274-282.
18. S. Belmares-Perales, M. Castro-Román, M. Herrera-Trejo and L. E. Ramírez-Vidaurri, *Met Mater Int* 2008, vol. 14, pp. 307-314.
19. Y Awano and Y Shimizu, *AFS Transactions* 1990, vol. 98, pp. 889-895.
20. Hyun You Kim, Sang Won Han and Hyuck Mo Lee, *Materials Letters* 2006, vol. 60, pp. 1880-1883.
21. M. Mahta, M. Emamy, A. Daman, A. Keyvani and J. Campbell, *Int J Cast Metal Res* 2005, vol. 18, pp. 73-79.
22. SS Sreeja Kumari, RM Pillai and BC Pai, *Journal of alloys and compounds* 2008, vol. 453, pp. 167-173.
23. FH Samuel, AM Samuel and HW Doty, *Transactions of the American Foundrymen's Society* 1996, vol. 104, pp. 893-902.
24. Salem Seifeddine, Sten Johansson and Ingvar L. Svensson, *Materials Science and Engineering: A* 2008, vol. 490, pp. 385-390.
25. Mousa Javidani, Daniel Larouche and X. Grant Chen, *Metall and Mat Trans A* 2015, vol. 46, pp. 2933-2946.
26. A. M. Samuel, J. Gauthier and F. H. Samuel, *Metallurgical and Materials Transactions a-Physical Metallurgy and Materials Science* 1996, vol. 27, pp. 1785-1798.
27. C. G. McKamey and J. A. Horton, *Metallurgical Transactions A* 1989, vol. 20, pp. 751-757.
28. A. R. Farkoosh, X. G. Chen and M. Pekguleryuz, *Mater. Sci. Eng. A-Struct. Mater. Prop. Microstruct. Process.* 2015, vol. 620, pp. 181-189.
29. A. R. Farkoosh, X. Grant Chen and M. Pekguleryuz, *Materials Science and Engineering A* 2015, vol. 627, pp. 127-138.
30. L. Anantha Narayanan, F. H. Samuel and J. E. Gruzleski, *Metall and Mat Trans A*

1994, vol. 25, pp. 1761-1773.
31. Jon Mikel Sanchez, Iban Vicario, Joseba Albizuri, Teresa Guraya, Natalia E Koval and Jose Carlos Garcia, *Metals-Basel* 2018, vol. 8, p. 167.
32. M. V. Kral, H. R. McIntyre and M. J. Smillie, *Scripta Materialia* 2004, vol. 51, pp. 215-219.
33. E. A. Elsharkawi, E. Samuel, A. M. Samuel and F. H. Samuel, *Journal of Materials Science* 2010, vol. 45, pp. 1528-1539.
34. M.V. Glazoff, V.S. Zolotorevsky and N.A. Belov: *Casting Aluminum Alloys*. (Elsevier Science, 2010), pp. 85-90.
35. K Liu, X Cao and X-G Chen, *Metallurgical and Materials Transactions B* 2012, vol. 43, pp. 1231-1240.
36. K. Liu, Hezhaoye Ma and X. Grant Chen, *Journal of Alloys and Compounds* 2017, vol. 694, pp. 354-365.

Caption of Figures:

**Fig. 1** Typical Fe-rich intermetallics (indicated by arrows) in: (a) Alloy H0, (b) Alloy L0, (c) Alloy Mn1, (d) Alloy LM2, and (e) Alloy Mn3.

**Fig. 2** TA curves of (a) Alloy L0 and (b) Alloy H0 as well as microstructure after interrupted water quench at: (c) 570°C and (e) 540°C of Alloy L0; (d) 570°C and (f) 540°C of Alloy H0 (black and white arrows indicate P-β-Fe and E-β-Fe, respectively).

**Fig. 3** Chinese Script Fe-rich intermetallic in Alloy Mn3 (a) and its EBSD pattern (b) as well as the simulation results (c)

**Fig. 4** TA curves of alloys: (a) LM3 and (b) HM3 and microstructure after interrupted water quench at 580 °C of (c) LM3 and (d) HM3 alloys (black arrows indicate α-Fe)

**Fig. 5** Optical micrographs showing effect of Mo on microstructure for low-Fe (0.3%) alloys: (a) L0, (b) LM1, and (c) LM3; for high-Fe (0.7%) alloys: (d) H0, (e) HM1, and (f) HM3 (white, blue dotted black, and thick black arrows indicate E-β-Fe, P-β-Fe, and α-Fe, respectively)

**Fig. 6** Area fractions of α-Fe, P-β-Fe, and E-β-Fe for different Mo additions in (a) Low Fe alloy, (b) High Fe alloy.

**Fig. 7** DSC heating curves of (a) low-Fe alloys, (b) high-Fe alloys and (c) enlarged zone 5 in (a) while (d) enlarged zone 4 in (b)

**Fig. 8** Optical images of alloys: (a) Mn1, (b) Mn2, (c) Mn3, and (d) Mn4 (white, black, and thick black arrows indicate E-β-Fe, P-β-Fe, and α-Fe, respectively)

**Fig. 9** Area fractions of α-Fe, P-β-Fe, and E-β-Fe in experimental alloys

**Fig.10** Correlation between Mo and Mn contents with area fractions of (a) P-β-Fe and (b) α-Fe in alloys with high Fe contents (0.7%)

Tables:

**Table 1** Chemical composition of the experimental alloys

| | Elements (wt. %) | | | | | | | |
|---|---|---|---|---|---|---|---|---|
| Alloy | Si | Cu | Mg | Ti | **Fe** | **Mo** | **Mn** | Al |
| L0 | 5.35 | 3.19 | 0.08 | 0.10 | **0.28** | 0 | 0 | Bal |
| LM1 | 6.00 | 3.36 | 0.09 | 0.16 | **0.32** | **0.19** | 0 | Bal |
| LM2 | 6.02 | 3.42 | 0.09 | 0.14 | **0.31** | **0.32** | 0 | Bal |
| LM3 | 5.92 | 3.44 | 0.09 | 0.13 | **0.31** | **0.37** | 0 | Bal |
| H0 | 5.81 | 3.28 | 0.10 | 0.11 | **0.64** | 0 | 0 | Bal |
| HM1 | 6.00 | 3.35 | 0.09 | 0.12 | **0.67** | **0.18** | 0 | Bal |
| HM2 | 5.94 | 3.32 | 0.07 | 0.10 | **0.65** | **0.30** | 0 | Bal |
| HM3 | 5.89 | 3.41 | 0.11 | 0.10 | **0.70** | **0.41** | 0 | Bal |
| Mn1 | 6.18 | 3.4 | 0.09 | 0.12 | **0.66** | 0 | **0.25** | Bal |
| Mn2 | 6.04 | 3.39 | 0.10 | 0.11 | **0.68** | **0.15** | **0.25** | Bal |
| Mn3 | 6.18 | 3.46 | 0.09 | 0.14 | **0.69** | **0.30** | **0.26** | Bal |
| Mn4 | 6.02 | 3.52 | 0.09 | 0.17 | **0.66** | **0.41** | **0.24** | Bal |

**Table 2** SEM-EDS results of the Fe-rich intermetallics shown in Fig. 1

| Morphology | Phase | Elements (at. pct.) | | | | |
|---|---|---|---|---|---|---|
| | | Al | Si | Fe | Mn | Mo |

| | | | | | | |
|---|---|---|---|---|---|---|
| Platelet | A | 68.8±3.9 | 17.7±2.4 | 13.5±2.1 | N/A | N/A |
| | B | 67.0±2.6 | 17.7±1.4 | 15.0±0.9 | N/A | N/A |
| Chinese Script | C | 68.4±1.0 | 12.4±1.0 | 10.8±0.9 | 8.4±1.3 | N/A |
| | D | 69.1±3.1 | 12.9±1.7 | 10.2±1.4 | N/A | 7.8±1.3 |
| | E | 68.2±4.8 | 12.4±5.1 | 10.5±1.5 | 4.2±1.0 | 5.1±1.0 |

712

713

714 **Table 3** Formation of Fe-rich intermetallics in experimental alloys

| Peak | Phases | Alloys |
|---|---|---|
| 4 | P-β-Fe | H0, HM1, HM2, Mn1, Mn2, Mn3 |
| 5 | E-β-Fe | All alloys except LM3, Mn4 |
| 6 | α-Fe | All alloys except H0 |

715